# Cavity quantum electrodynamics with quantum dots in microcavities

Gudat, J.

# Chapter 4

# Microcavity Tuning

This chapter is based on three publications:

*Tuning micropillar cavity birefringence by laser induced surface defects* (C. Bonato, D. Ding, J. Gudat, S. Thon, H. Kim, P.M. Petroff, M. P. van Exter, and D. Bouwmeester, Appl. Phys. Lett. 95, 251104 (2009)) [71],

*Permanent tuning of quantum dot transitions to degenerate microcavity resonances* (J. Gudat, C. Bonato, E. van Nieuwenburg, S. Thon, H. Kim, P. M. Petroff, M. P. van Exter, and D. Bouwmeester, Appl. Phys. Lett. 98, 121111 (2011)) [72] and

*Strain tuning of quantum dot optical transitions via laser-induced surface defects resonances* (C. Bonato, E. van Nieuwenburg, J. Gudat, S. Thon, H. Kim, M. P. van Exter, and D. Bouwmeester, Phys. Rev. B, 84, 075306 (2011)) [73].

In our hybrid scheme for quantum information processing the photon's polarization degree of freedom encodes the qubit. This qubit must become entangled with an electron-spin qubit through the interaction via a cavity. Consequently the interaction must work for any polarization/spin state.
This translates into the following requirements:

1. The fundamental cavity mode of the microcavity needs to be polarization-degenerate.

2. The frequency of the two level system transition (a single quantum dot with a ground state and an excited trion state) and the polarization-degenerate fundamental cavity mode must be in resonance.

Fabrication of the oxide-apertured micropillar structures with embedded QDs is a difficult and complex process. Currently, it is impossible to obtain the properties deterministically in the fabrication process. Even if in the unlikely

case of fulfilling both requirements, fine-tuning of the properties can yield increased performance. In this chapter we will address important details on the sample design and fabrication and the possibilities to reduce the polarization splitting of the fundamental mode before applying tailoring methods. We first demonstrate how we can tune the cavity mode frequency. The second tuning method describes the possibility to shift the QD optical transition. A theoretical model is developed that explains the experimental results qualitatively.

## 4.1 Introduction

Different methods for permanently or reversibly tuning cavity structures have been developed. The motivation of these methods is to enhance the spontaneous emission of a light source embedded in the cavity, described by the Purcell factor (see Chap. 1 Sect. 1.5.6). Self-assembled QDs in microcavities are grown epitaxially where the lattice mismatch (see Chap. 1 Sect. 1.3.2) leads to an inherent build up of elastic strain energy. The formation of the strained islands, during which process the elastic strain energy minimizes, and the following capping with a larger bandgap material is non-deterministic. Consequently, the optical properties determined by the composition, the size, and the local strain of the QD can only be controlled to a certain degree. Particularily, we have control over the wavelength range of several nanometer that the QD will emit at. However, precise matching of the optical transition frequency of the QD with the cavity mode resonance frequency is crucial [41].

Matching of the frequencies can be achieved by tuning either the cavity, the QD, or both. For photonic crystal cavities several techniques have been developed shifting the cavity resonance. These are wet chemical digital etching [74], photodarkening of a thin chalcogenide glass layer [75] or a photochromic thin film [76] deposited on top of the device, atomic force microscope nano-oxidation of the cavity surface [77], infiltration of liquids [78, 79] or absorption of xenon [80]. In comparison to micropillar cavities where the cavities are covered by layers of DBR mirrors, the cavities are directly accessible in photonic crystals. Therefore it needs other tuning techniques.

One possibility is to shift the QD transition in frequency. Embedding the QD in a diode structure allows to shift the frequency via the quantum confined Stark effect [81, 82](see Chap. 1 Sect. 1.3.4). This technique is limited by a tuning range of hundreds of $\mu$eV. QD optical transition shifts in the order of 1meV can also be achieved by temperature tuning the micropillar [39, 83]. Here, the cavity mode also shifts with the temperature (5$\mu$eV/K) but less than

the QD ($40\mu$eV/K) transition [5]. The disadvantage of temperature tuning is the reduced signal emitted by the QDs with increasing temperature.

A blueshift of the QD transition can be obtained through local annealing of the QD composition [84]. The induced heat caused by a focused laser beam can control the intermix of the indium atoms of the QD with the gallium atoms of the surrounding material.

A focused laser is also used in our technique. But instead of annealing the QD, we create small defects on the sample surface near the micropillar cavity region, distant enough to preserve the optical quality of the cavity. The creation of strain can alter the optical properties of the QD and the cavity as has been investigated utilizing piezoelectric actuators or mechanical tips [85–88]. This fact can be exploited to change the birefringence of the cavity in a controlled way such that the fundamental mode of the cavity becomes polarization-degenerate. In addition, we developed a technique to fine-tune the optical properties of self-assembled QDs by strain perturbation also given by laser-induced surface defects. The advantages of our approach is the permanent tuning of the sample properties.

## 4.2 Oxide-apertured micropillar design and properties

In the previous chapter we focused on explaining the mode profile that the oxide-apertured micropillar exhibit. We pointed out the importance of the oxide-aperture structure for understanding the modes. This chapter emphasizes different design considerations to achieve polarization-degeneracy and the possibility to electrically address the QDs.

Figure 4.1 shows a sketch of the micropillar scheme. The micropillars are grown by molecular-beam epitaxy on a GaAs [100] substrate. The bottom distributed Bragg reflector (DBR) mirror consists of 32 pairs of the alternating layers of GaAs (68.4nm) and $Al_{0.9}Ga_{0.1}As$ (79.8nm) corresponding to a one-quarter optical thickness, with a total thickness of $4.8\mu$m each. The active cavity layer is $\lambda$-thick with two layers of GaAs ($2 \cdot 135.4$nm) that embed the InGaAs/GaAs QDS in the center. The QDs are self-assembled as described by the Stranski-Krastanow forming InGaAs islands. The density of the QDs can be controlled though the positions of the islands form randomly. (For an active way of positioning the QDs see the next chapter.) The islands are partially covered with GaAs and annealed before completely capped with GaAs causing

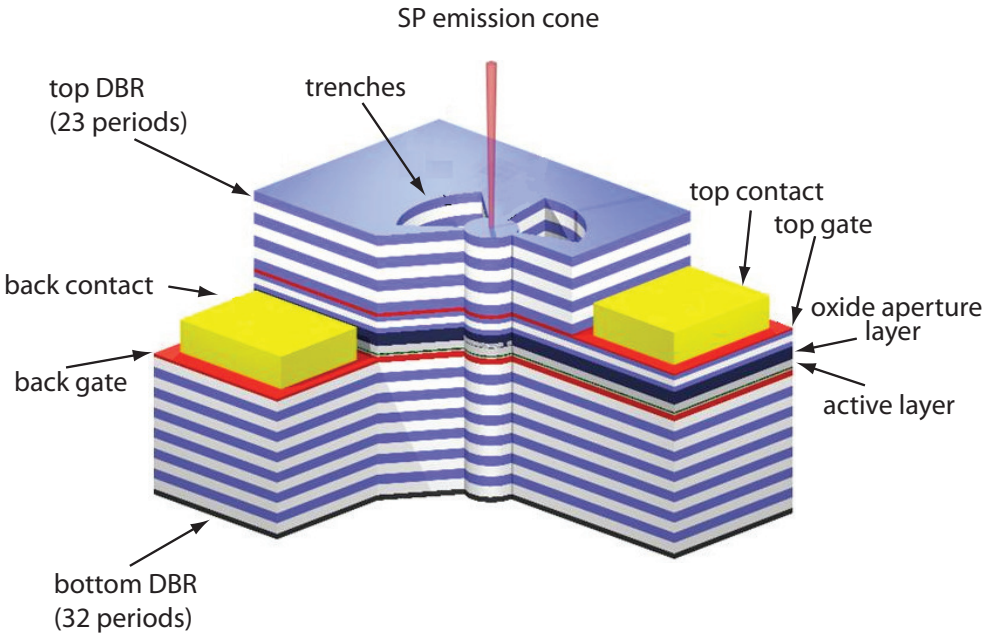


Figure 4.1: *Sketch of the micropillar structure.*

a blue-shift of the QD's emission wavelength [89]. The oxide aperture layer on top of the active region has a thickness of $3/4\lambda$. The layer is composite of pure AlAs and sandwiched between $Al_{0.89}Ga_{0.11}As$ and $Al_{0.75}Ga_{0.25}As$. The top DBR has 23 pairs of the same alternating layers as the bottom DBR which leads to a thickness of $3.5\mu$m. Trenches are etched through the sample approximately $4.3\mu$m deep so that they reach the active region. The micropillar structures are typically $30\mu$m in diameter and are very robust. They include electrical gates [56] for controlled electron charging of the QD and fine tuning of the frequency via the Stark effect.

The micropillar cavities exhibit materials that have an anisotropic characteristic. This anisotropy causes birefringence meaning polarization dependance of the light passing through the material. The oxidation front forming the oxide aperture has a large influence on the birefringence. That is partially caused by the different anisotropic growth-rate of the oxide and the asymmetries in the shape and position of the trenches [64, 65].

Before applying any tuning techniques, we aim to fabricate microcavities with their fundamental mode splitting being as small as possible. For this purpose various geometries of the trench design were explored leading to a

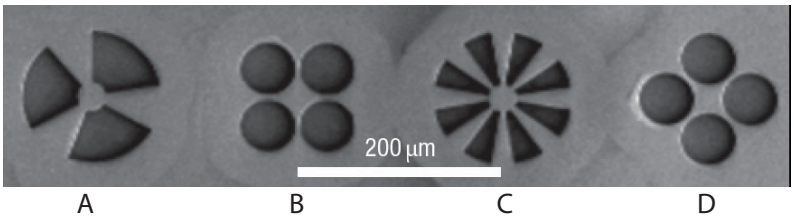


Figure 4.2: *SEM top view of various geometries for cavities with a different trench design. The design have in common that their inner lateral cavity area has a diameter of* $20\mu m$.

polarization splitting as small as 50GHz [56], see Fig. 4.2. Additionally, the density of QDs has to be very low, so that we can address and identify single QD transitions.

From the different geometries shown in Fig. 4.2 we only worked with samples with three or four trenches shaped as in Fig. 4.2(a). Optimized initial splittings for these cavities are achieved by varying the relative position of the trenches of one cavity. One trench is relatively positioned toward or outward the center along the crystal axis of the substrate by a few hundred nanometers up to a few microns. In this way, fabrication allows to get cavities with their fundamental mode splitting being smaller than 0.03nm in wavelength (corresponding to 10GHz). Only then, during the active tuning in the second step which is described in detail in the next section section, the tuning-range of a few Angstroms is enough to achieve polarization degeneracy.

## 4.3 Tuning micropillar cavity birefringence by laser induced surface defects

In the following we describe how to permanently modify the birefringence of the cavity in a controlled way allowing to shift the two polarization modes almost independently. The tuning mechanism is so accurate that a polarization-degenerate cavity can be achieved. We define polarization-degeneracy when the fundamental mode splitting of the cavity is less than 0.2nm. This matches the spectral emission bandwidth of our QDs.

In order to permanently change the birefringence of the cavity we create permanent surface defects near the cavity by focusing a strong laser beam on the sample. This results in local melting of the material creating a hole with some material accumulated around the edge of the hole. As a consequence of

the hole the strain in the structure is affected which itself changes the birefringence. The magnitude of the induced stress varies with the laser power applied and its exposure time. The orientation of the effect is determined by the position of the burned hole in respect to the cavity center and the trenches.

Originally, the technique described was developed to tune the polarization properties of vertical-cavity surface-emitting lasers (VCSEL) [90, 91]. Compared to the other techniques like temperature tuning [5] or Stark shift tuning [92] our method has a permanent effect.

### 4.3.1 Experimental procedure

In the first step, we pre-select cavities with a reasonable small polarization splitting of the fundamental mode ($< 20$GHz). For creating surface defects we utilize a Ti-sapphire laser approximately applying 250mW power tuned to 770nm in order to have sufficient absorption by the semiconductor material. The laser is tightly focused on the sample by a high numerical aperture (NA) aspheric lens $L_1$ (focal length $f_0 = 4.02$mm, NA$= 0.6$). Precise positioning on the sample is achieved by imaging the sample surface through an optical system consisting of the focusing lens $L_1$ and a second lens $L_2$ with a focal length $f = 150$mm onto a charge-coupled device (CCD) camera placed in the focal plane of the $L_2$. (See Chap. 2 for more details.) Through visual inspection we determined the power and the time needed to sufficiently induce surface defects. Typically the resulting holes are $3 - 5\mu$m wide with a varying depth of 30nm to $2\mu$m. See Fig. 4.3 for an atomic force microscopy (AFM) image of a typical hole. The hole has a depth of $2.28\mu$m and an approximate diameter of $3\mu$m. The laser induced impact has been between 30s to 1min. The results and the data provided were carried out at room temperature. At lower temperatures i.e. at 4K the power has to be increased to achieve similar effects on the surface. At 4K we utilized a laser with 500mW at 532nm.

Choosing the right position to burn a hole is the crucial step to iteratively get to a point where the splitting of the fundamental mode is reasonable small. Based on initial tests on different cavities and ideas originally developed to tailor the polarization properties of vertical-cavity surface-emitting lasers [90, 91], locations are determined on the basis of the expected angular and $1/r$ dependence of the induced strain. $r$ is the distance from the cavity center and is always chosen large enough to be a few microns away from the center of the micropillar cavity in order not to reduce the optical quality of the cavity.

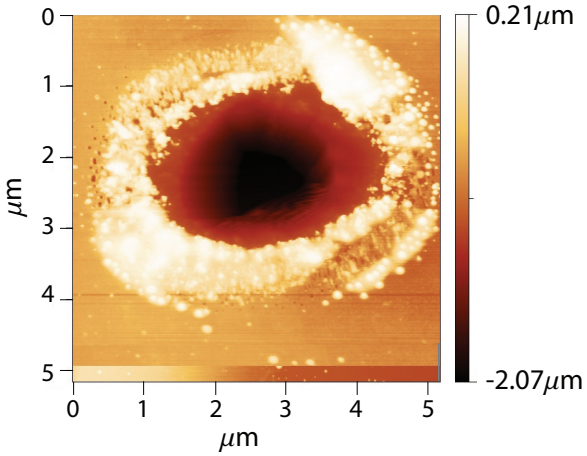


Figure 4.3: *AFM image of a typical hole. The hole has a depth of* $2.28\mu m$ *and an approximate diameter of* $3\mu m$.

### 4.3.2 Data analysis

The fundamental transverse cavity mode exhibits a very good spatial Gaussian shape (see previous Chap. 3). The mode divides into two orthogonally-polarized submodes ($M_A^{[00]}$ and $M_B^{[00]}$). In order to analyze the changes in the splitting of the fundamental mode we pump the semiconductor material above the bandgap with a Ti-Sapphire beam of a few mW. The cavity-shaped photoluminescence is recorded on a spectrometer with a resolution of 5.5GHz/pixel on the attached CCD array. The polarization dependence of the whole spectrum and in particular the fundamental mode is characterized by placing an analyzer consisting of a fixed linear polarizer and a rotating half-wave plate in front of the spectrometer. This assures the polarization state in the spectrometer to be constant and so that the measurements are not affected by the polarization dependent response of the grating.

The spectral splitting of the fundamental mode can be very small, less than 1GHz. But even when being a few GHz the two orthogonal fundamental modes $M_A^{[00]}$ and $M_B^{[00]}$ are overlapping on the spectrometer and their different peaks cannot be observed directly. But because the modes are orthogonally polarized a polarizer in the collection path allows to maximize the signal for each mode separately. When the signal from $M_A^{[00]}$ is optimized at an angle $\theta_A$ at frequency $\nu_A$, mode $M_B^{[00]}$ is best observed at frequency $\nu_B$ at $\theta_B + \pi/2$. The shift between the two peaks is periodical with rotation of the polarizer. An important analysis tool is additional Lorentzian fitting of the peak (see Fig.

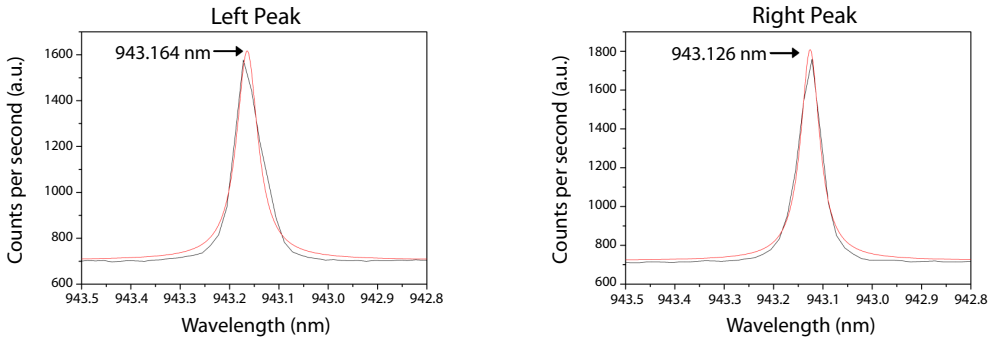


(a) (b)

Figure 4.4: *Initial splitting of the fundamental mode and Lorentzian fitting for the left (a) and the right (b) peak.*

4.4). The highly increased resolution allows to determine splitting of less than 0.1GHz. Figure 4.5(a) illustrates the periodic behavior of the fundamental mode frequency when rotating the polarization analyzer. For the curve with the dotted line the central frequency separation of the two modes is $\Delta\nu = 13.7 \pm 0.3$GHz with a $FWHM$ of $30.1 \pm 0.4$GHz for a single polarization mode.

Successive burning does not necessarily always lead to a decrease in splitting. But with initial tests on other cavities on the same sample, holes are burned at locations with an expected angular and $1/r$ dependence of the induced strain. Figure 4.5(a) shows how the splitting reduces to $\Delta\nu = 2.0 \pm 0.2$GHz after four holes were burned on the same cavity. The holes were induced in the order as seen in Fig. 4.5(b). The first hole was positioned close to the cavity center which caused a reduction of the splitting from 13.7±0.3GHz to $6.1 \pm 0.7$GHz. As the second hole did not reduce the splitting much further, two more holes were burned much closer to the center of the cavity, namely along the edge of the eastern trench. All holes were burned for one minute.

For establishing a better understanding of the frequency shift we analyzed many more cavities burning a couple of hundreds of holes trying different sequences of positions. These tests were all carried out at room temperature as there was no need to observe the effects on the QDs (apart from making sure the burning does not destroy the active emitters) yet. Figure 4.6 is an example for a set of trials illustrating the positions of the holes burned chronologically numbered from 1 to 24. The two resulting polarization peaks $\lambda_A$ and $\lambda_B$ are plotted in Fig. 4.7 for each position on the horizontal and vertical axes.

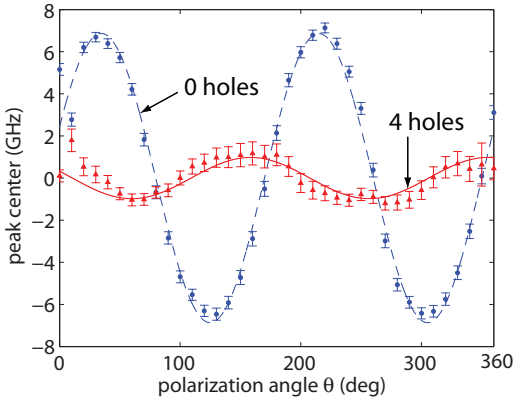


(a) Periodic oscillations of the peak center.

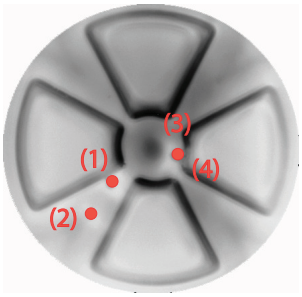


(b) Sequence of four induced holes.

Figure 4.5: *(a) Periodic oscillations of the peak center as a function of the analyzer angle. The dotted curve shows the results for no holes burned yet. Unaltered, the splitting is* $\Delta\nu = 13.7 \pm 0.3 GHz$*. After four holes induced holes (b) the splitting (solid line) is reduced to* $\Delta\nu = 2.0 \pm 0.2 GHz$*. The holes were all burned for one minute. The closer the hole is located to the center of the cavity the larger were the changes in the splitting.*

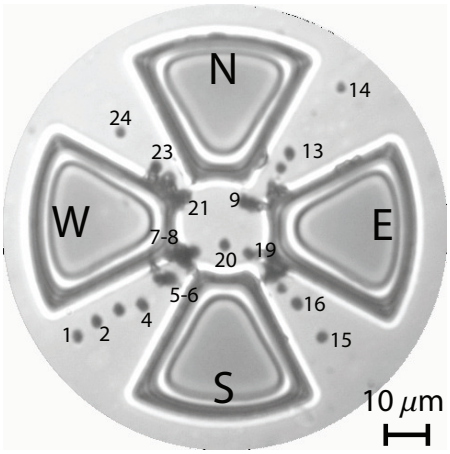


Figure 4.6: *Sequence of 24 hot spots burned. Optical microscope image of a micropillar cavity with hot spots burned on the structure in the regions between the trenches. The numbers refer to the chronological order in which the holes were burned.*

The first eight holes were burned between the southern and the western trench moving from the outside closer to the center of the cavity to be continued with six more holes on the other side moving from the center outwards between the northern and the eastern trench. This line goes along with the [001] crystal lattice orientation.

At the beginning $\lambda_B$ and $\lambda_A$ shift relatively little before the smallest splitting of $\Delta\nu = 3.2 \pm 0.4$GHz is measured after hole five (compare the spectrum of both overlapping modes in the inset of Fig. 4.7). Getting closer to the center, the frequency shifts are much larger with $\lambda_A$ increasing more than $\lambda_B$. After hole 14 the splitting has increased to $\Delta\nu = 108 \pm 1$GHz. Orthogonal positioning of the hole shifts the frequency $\lambda_B$ much faster than $\lambda_A$.

The tests on this cavity demonstrate that it is possible to almost independently tune the frequency of each polarization mode by more than a 100GHz by wisely choosing the position relatively to the center of the cavity. The orientation with respect to the crystal lattice is a measure for which mode is preferably tuned. The distance from the center of the cavity is a measure for the strength of the effect. The closer the hole is burned the more do the frequencies shift.

Before elaborating on the theoretical model described in the next section, it is useful to explain the effect of holes burned with a simple model, based on the tensorial relationship between stress, strain and the optical properties

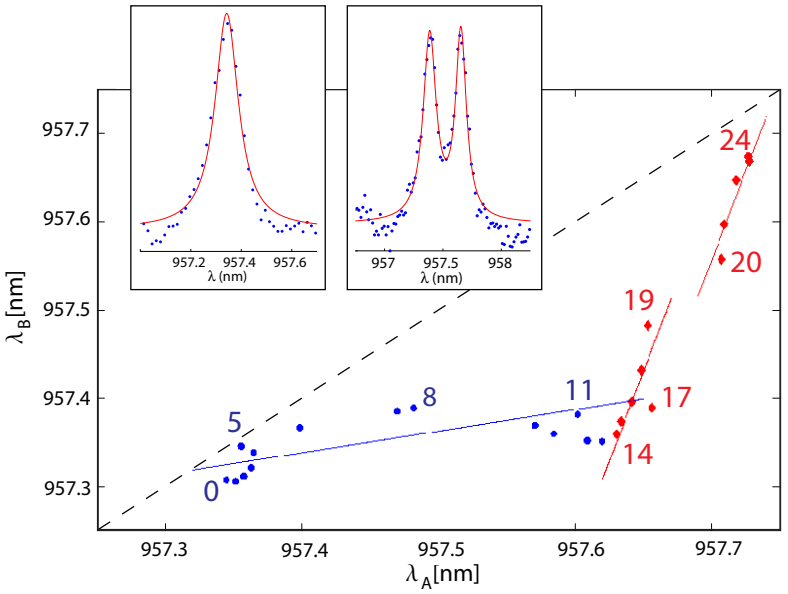


Figure 4.7: *Frequency shift of each submode when positioning the holes as illustrated in Fig. 4.6. The small insets show extreme splittings in the total spectrum. The splitting reduced to* $\Delta\nu = 3.2 \pm 0.4 GHz$ *after five holes. After 14 holes the splitting is* $\Delta\nu = 108 \pm 1 GHz$.

of the material. Essentially, the anisotropic component of the stress changes the splitting and the isotropic component affects the absolute frequencies of the two submodes. In particular, we find that for $N$ holes burned along the $x$ direction:

$$n_B^{(N)} = n_0 + \left(n_A^{(N)} - n_0\right)\left(-\frac{\Pi_2}{\Pi_1}\right), \tag{4.1}$$

which corresponds to a straight line with slope $\rho_1 = -\Pi_2/\Pi_1$. $\Pi_1$ and $\Pi_2$ are quantities which depend on the tensorial elastic ($C_{ij}$) and and elasto-optic ($\rho_{ij}$) coefficients of the material ($\Pi_1 = p_{11}C_{11} - p_{12}C_{12}$ and $\Pi_2 = p_{11}C_{12} - p_{12}C_{11}$). For the holes burned along the $y$ direction we find a similar linear relationship with inverted slope $\rho_2 = -\Pi_1/\Pi_2$. Figure 4.7 shows how well this simple model fits the data. The slope for the fitted line is $4.0 \pm 0.5$. Literature values for the bulk GaAs and AlAs thermal and elasto-optic properties [93] give a slope of around 1.5. However, we do not expect these values to be perfectly compatible since our model does not take into account the bimorphic structure formed by the oxidized AlAs layer and by the DBR mirrors.

So far we presented results for measurements performed at room temperature. Cavity resonance frequency and polarization splitting for holes burned at 4K show values significantly different from the room-temperature ones. Immediate hole-burning on the same structure at low-temperature, the burning laser power had to be increased to 500mW (532 nm). Polarization degeneracy could be achieved as well as frequency tuning, albeit with a different slope $\rho_2 = 1.2 \pm 0.5$. The stability of the effects was tested by warming up and cooling down the device a few times. A difference of the order of 10% was found for the first cooldown after burning (consistent with the results in [91]), while the deviation in the splitting is within $1 - 2$GHz for successive cool-downs.

### 4.3.3 Summary and outlook

We introduced a technique to permanently tune the polarization and spectral properties of optical micropillar cavities. By laser-burning a small defect on the sample surface near the cavity, we can induce a controllable amount of birefringence in the structure. By adjusting the position of the defect, we control the central wavelength of each of the two polarization submodes of the fundamental cavity mode. This technique enables the implementation of polarization-degenerate semiconductor micropillars for quantum information processing and it may find applications for fine tuning of other kinds of semiconductor microcavities whose optical properties are influenced by material strain, such as photonic crystal defect cavities and microdisk cavities. So far,

we have not shown how this method affects the emission of the QDs. This is the topic of the next section.

## 4.4 Permanent tuning of quantum dot transitions to degenerate microcavity resonances

The second requirement for implementation of quantum information schemes is spectral resonance between a polarization-degenerate micropillar cavity mode and an embedded QD transition. The method demonstrated in this section serves as the coarse-tuning technique to meet the requirement. Fine-tuning and selection of different charged states [94] is provided by the quantum confined Stark effect [81], applying a voltage to the PIN-diode structure that embeds the QDs (see Sect. 4.2). The combination of both the coarse and fine-tuning technique has many advantages. Different charged states can be addressed and it is possible to switch between these. The energy shifts can be tuned very precisely with a range up to a few hundred $\mu$eV. The coarse tuning method is based on the controlled manipulation of the isotropic and anisotropic tensile strain effected by laser-induced surface defects. The method is ideal for scalable purposes as the defects are permanent and no further external tuning equipment for further experiments is required.

### 4.4.1 Experimental procedure

Because of the non-deterministic character of the fabrication process, potential cavity candidates for further tuning are identified. For that purpose voltage-resolved photoluminescence scans (see Fig. 4.9 for a non-polarization resolved cavity scan) for each cavity are taken, providing information about spectral positions of QDs and the splitting of the fundamental mode. Promising candidates have single QDs spectrally close to the fundamental mode of the cavity which exhibit already a small splitting. Initial spectral overlap of the QD transition and the fundamental mode is not required. The spatial position of the QD with respect to the center of the cavity is of high importance. (An elaborate analysis of this fact is discussed in Chap. 8 on page 173.) Therefore we choose cavities that already exhibit a reasonable high count rate (compared to other cavities investigated) when the QD tunes into resonance with the fundamental mode.

Once a promising cavity QD system has been selected, the actual tuning technique can be applied. For that purpose we induce surface defects by a laser beam in the same way as in the previous section. Because we operate at 4K in

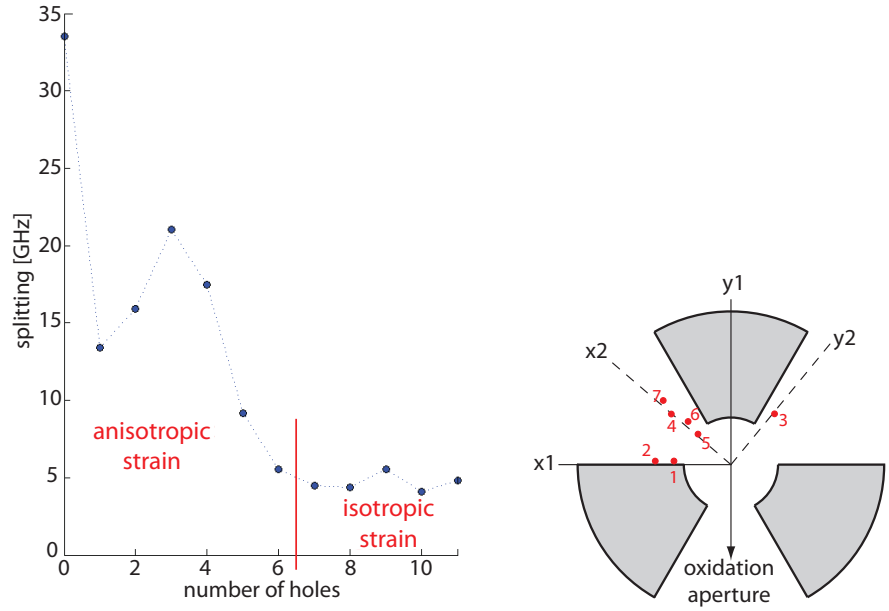


(a) (b)

Figure 4.8: *(a) Frequency splitting of the two orthogonally-polarized submodes of the fundamental cavity mode as a function of the burned holes. (b) Chronological order of holes burned.*

order to observe luminescence of the QD, we apply approximately 100mW/$\mu$m$^2$ at $\lambda = 532$nm tightly focusing the laser on the surface for 30s. For these measurements a high-NA aspheric lens L1 (focal length $f_0 = 4.2$mm, NA$= 0.6$) is mounted in the He-flow cryostat. The material is locally melted and evaporated, leaving a hole which is approximately 2$\mu$m wide and at least 2$\mu$m deep.

In the following we will describe the overall tuning technique by means of one single cavity (with three trenches). In a first step we reduce the fundamental cavity mode to polarization-degeneracy following the procedures described in the previous section. The built-in strain can be compensated by applying anisotropic strain, through holes burned at proper positions. The direction of the original built-in strain is however unknown, so one must use a trial-and-error procedure, illustrated in Fig. 4.8(a). We first start burning a hole at a random orientation, for example along the direction labeled in the figure as $x_1$. If the splitting gets larger, we move to the orthogonal direction. If the splitting decreases, we keep burning holes until the splitting stops decreasing. In the

example shown in Fig. 4.8(b), the first hole reduces $\Delta E$ from $140 \pm 4\mu$eV to $54 \pm 1\mu$eV, but a second one slightly increases it. This is an indication that all the strain along that particular direction was compensated. We repeat the same procedure on a reference system rotated by 45 degrees with respect to coordinate plane $[x_1, y_1]$. In the example, we start burning the third hole along $y_2$, which increases the splitting to $\Delta E = 82.6 \pm 0.4\mu$eV. Therefore we switch to the orthogonal direction $x_2$. Burning holes along this direction reduces $\Delta E$ to around $15\mu$eV. The procedure can be further iterated along directions in between $x_1$ and $x_2$ and generally leads to splittings smaller than the mode linewidth (in our system about $50\mu$eV), which is the requirement for quantum information experiments. It is important to note, that no appreciable change in the cavity quality factor was observed.

So far we only concentrated on tuning the fundamental mode to polarization-degeneracy. However, the strain affects the optical transitions of the QDs as well. For the same cavity analyzed in Fig. 4.8, Fig. 4.9 shows the voltage-resolved photoluminescence at the initial state before any holes are induced. The sample is non-resonantly pumped with a $1\mu$ mW/$\mu$m$^2$ laser beam at 785nm above the GaAs bandgap. The photoluminescence is spectrally resolved with a spectrometer (resolution 0.016nm/pixel). The non-degenerate cavity's fundamental mode splitting ($140\mu$eV) is clearly visible as different horizontal lines around 943.1nm. QD transitions shifting in frequency due to the Stark effect and tuning into the different modes can be tracked by the curved lines. Though there are more than three QDs visible, we only marked three clearly visible QDs. $QD_3$ is around 0.5meV detuned to the blue-side of the cavity mode.

The summary of the effects of the 12 holes burned is shown in some of the voltage-resolved photoluminescence plots in Fig. 4.10 and Fig. 4.11. Burning 6 holes reduces the splitting to about $15\mu$eV and $QD_3$ is about 0.1meV detuned. Applying isotropic strain, by burning pair of holes along orthogonal direction, the dot can be brought into resonance with the cavity mode, without destroying the mode degeneracy (see plot for 11 holes in Fig. 4.11).

The difference in the way the cavity mode and the dot transition are affected by hole-burning can be exploited to tune a QD transition into resonance with a polarization-degenerate cavity. In Fig. 4.10 one can see that, while burning the first six holes, needed to reduce the splitting $\Delta E$, the optical transitions of the dots redshift, so that the transitions labeled as $QD_1$ and $QD_2$, originally resonant with the non-degenerate fundamental cavity mode, tune out of resonance. After burning six holes we have a polarization-degenerate cavity mode, with a QD transition (labeled $QD_3$) about $100\mu$eV detuned on the blue-side. Now the challenge is to shift this transition into resonance, without perturbing the cavity mode degeneracy. This can be done by applying isotropic

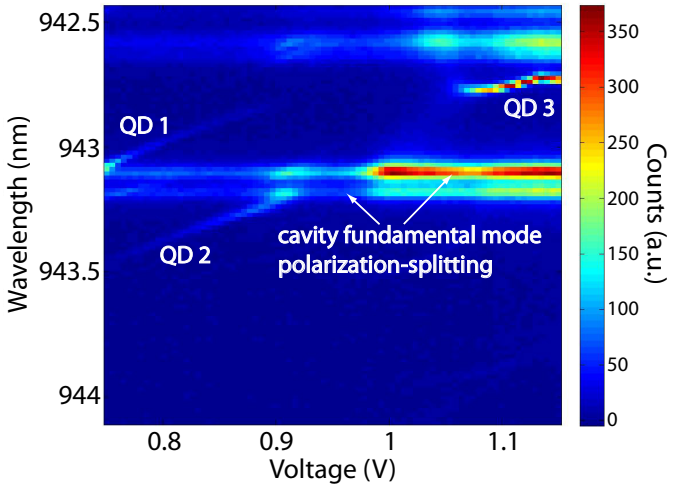


Figure 4.9: *Voltage-resolved photoluminescence plot before inducing any holes. The scan is non-polarization resolved and non-normalized. The curved lines are characteristic for QDs. The horizontal lines are the cavity modes.*

strain: we can burn sets of two holes at orthogonal directions, for example one along $x_2$ and the other along $y_2$, at the same distance from the center. This leaves the splitting $\Delta E$ unaltered while redshifting the dot transition. The results are shown in Fig. 4.11(c) and Fig. 4.11(d) corresponding to the eleventh and twelfth hole burned. The dot is finally on resonance and the fundamental cavity mode splitting is $13 \pm 1\mu$eV.

For a better understanding of how the QD shift spectrally after a new hole is burned, we kept track of its frequency shift by recording voltage-scans. In general, the resulting shifts to higher wavelengths was studied in many nominally identical cavities and show the behavior as presented for one cavity in Fig. 4.12(a). The effect of laser-induced defects is almost always a redshift of the optical transition, independent of the actual position of the hole. This fact has been observed by other groups as well [95–97] and suggests that by burning holes we effectively apply tensile strain to the structure.

As we usually have a couple of QDs active in the same cavity, it is interesting to measure all their relative shifts in energy after a new hole is burned. Figure 4.12(b) presents the tracking of energies for four QD optical transitions with respect to their original energies when six holes are burned at the same distance from the cavity center but at different positions. Independently of the angle along which the hole is burned, the QD emission always redshifts.

In our measurements we found the shift of the QD transition to be much

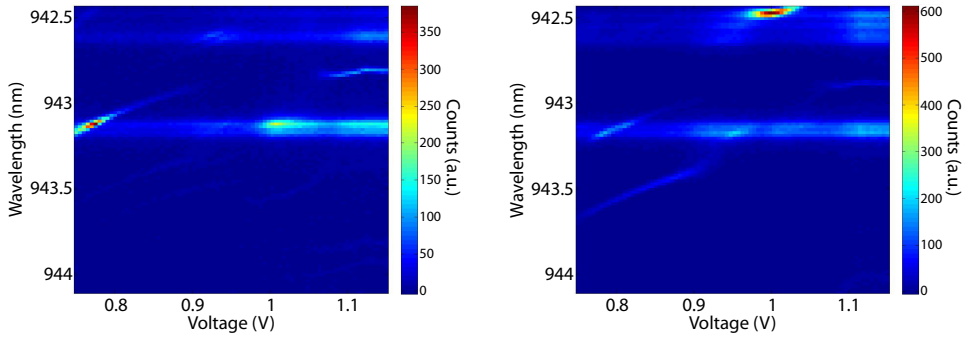


(a) 1 hole




(b) 2 holes

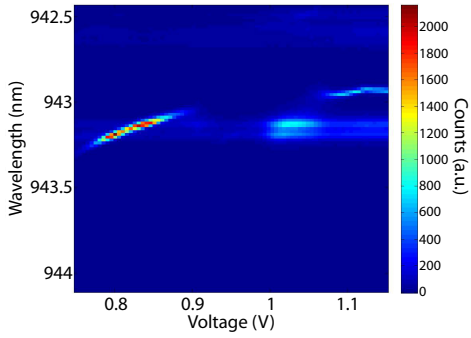


(c) 3 holes

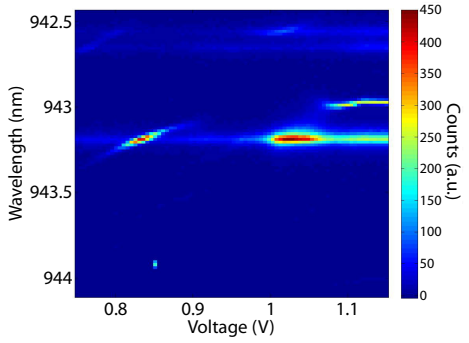


(d) 4 holes

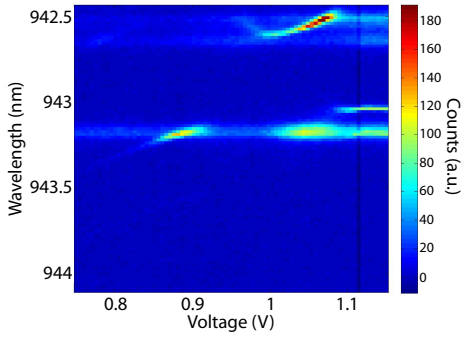


(e) 5 holes

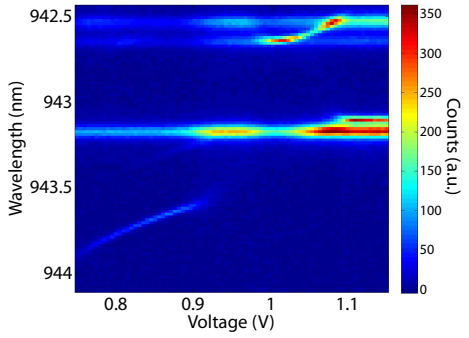


(f) 6 holes

Figure 4.10: *Hole burning applying anisotropic strain. The result is a reduction of the fundamental mode splitting.*

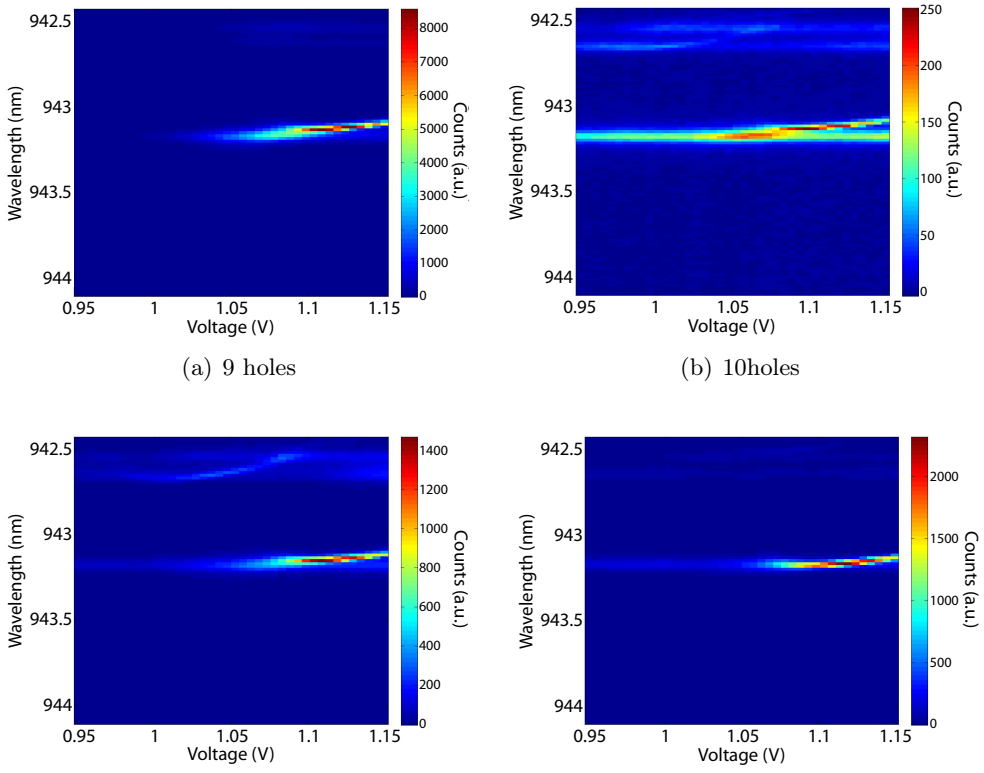


(a) 9 holes

(b) 10holes

(c) 11 holes

(d) 12 holes

Figure 4.11: *Hole burning applying isotropic strain. The QD transition redshifts till it is in resonance with the fundamental mode of the polarization-degenerate cavity.*

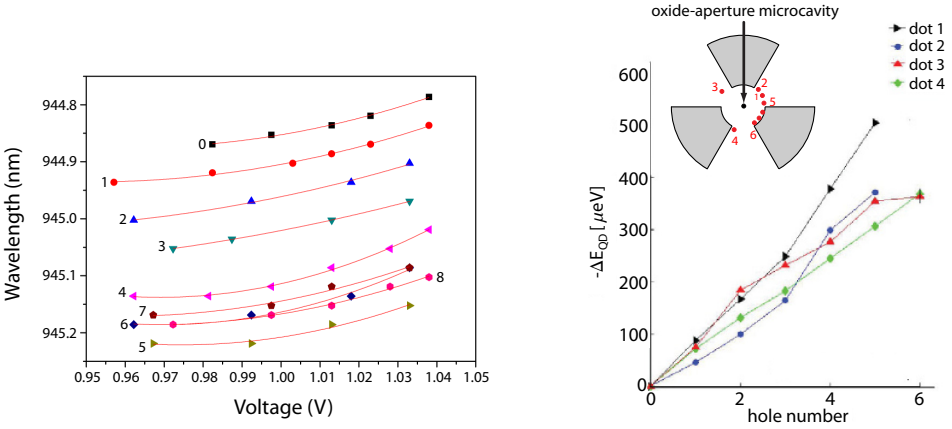


(a) (b)

Figure 4.12: *(a) Voltage-resolved shifts for different holes burned for one QD. With almost every new hole induced, the QD emission redshifts (increasing wavelength). (b) Tracking the energy for four different QD optical transitions for six holes burned. The energies are plotted with respect to their original energy. The holes are burned at the same distance from the cavity center (see inset). All transitions always redshift (decreasing $\Delta E_{QD}$) independently of the orientation of the hole position with respect to the cavity and the crystal axes.*

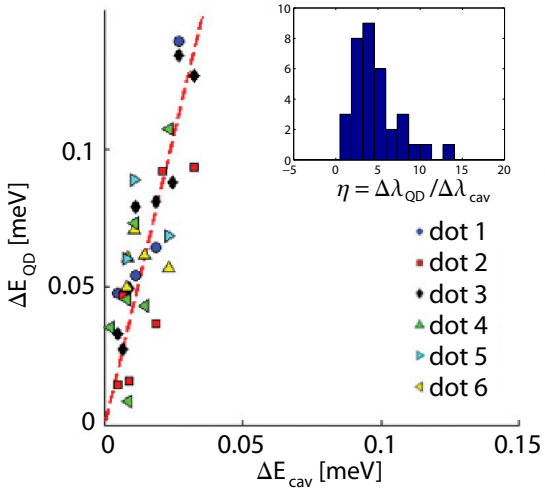


Figure 4.13: *Energy shifts for a QD optical transition and the optical cavity mode for six different QDs. The dotted (red) line is a linear fit. The inset shows a histogram of the ratios between the shift of the QD and the shift of the cavity mode. On average the QD frequency shifts around 5 times more than the cavity resonance.*

larger than the corresponding shift of the cavity mode. Figure 4.13 provides a quantitative analysis of this phenomenon. It shows the energy shifts for a QD optical transition and the optical cavity mode for six different QDs. The dotted (red) line is a linear fit. The inset shows a histogram of the ratios between the shift of the QD and the shift of the cavity mode. On average the QD frequency shifts around 5 times more than the cavity resonance.

### 4.4.2 Summary

We demonstrated a tuning technique for micropillar cavities with embedded QDs, which allows us to obtain polarization-degenerate micropillars with a QD transition on resonance. Our technique is a crucial prerequisite for the implementation of scalable quantum information systems involving photon polarization and the spin of a single carrier trapped in the dot. We showed that the QD optical transition redshifts, independently of the actual position of the hole. The QD frequency shift is about five times larger than the shift of the cavity fundamental mode.

## 4.5 Theoretical model

A model that describes the effect of introducing strain through local heating in the vicinity of the device is proposed by van Doorn *et al.* [98] for VCSEL structures. The approach is to calculate the thermal expansion due to a point heat source in a bulk material. With the relation of the temperature of the point heat source and the elastic properties of a hole burned at position $(x_0, y_0, 0)$, the stress component $\sigma_{ij}$ at position $(x, y, z)$ can be calculated as follows ($x_i = x, y, z$): [98]

$$\sigma_{ij} = \gamma \frac{A_0}{r} \left[ \delta_{ij} - \frac{(x_i - x_i^{(0)})(x_j - x_j^{(0)})}{r^2} \right], \tag{4.2}$$

with $x - x_0 = r\cos\theta\cos\varphi$, $y - y_0 = r\sin\theta\cos\varphi$ and $z - z_0 = r\sin\varphi$. $\gamma$ describes the elastic composition of the material with $C_{ij}$ being different elastic constants:

$$\gamma = \frac{(C_{11} - C_{12})(C_{11} + 2C_{12})}{C_{11}} \tag{4.3}$$

$A_0$ is a phenomenological coefficient, of dimension length, which depends on the laser power and on the thermal expansion coefficient and thermal conductivity of the material. For compressive stress $A_0$ is positive and negative for tensile stress. The factor $1/r$ attributes a decreasing effect from the hole.

We have experienced that a certain laser power and burning time is needed to obtain a permanent and irreversible effect, parameters that also depend on the cooling temperature of the sample and the quality of the focus. In this approach we assume that the stress caused by laser-induced defects has the same form for reversible and permanent defects as described in Eq.(4.2). The stress induced causes strain (tensor $\varepsilon_{kl}$) in the crystal lattice, that can be described by elastic compliance tensor with components $s_{ijkl}$:

$$\varepsilon_{ij} = s_{ijkl}\sigma_{kl}. \tag{4.4}$$

For a GaAs crystal with a $4\bar{3}m$ trigonal crystal, a matrix representation is:

$$S = \begin{bmatrix} S_{11} & S_{12} & S_{12} & 0 & 0 & 0 \\ S_{12} & S_{11} & S_{12} & 0 & 0 & 0 \\ S_{12} & S_{12} & S_{11} & 0 & 0 & 0 \\ 0 & 0 & 0 & S_{44} & 0 & 0 \\ 0 & 0 & 0 & 0 & S_{44} & 0 \\ 0 & 0 & 0 & 0 & 0 & S_{44} \end{bmatrix}, \tag{4.5}$$

where the coefficients $S_{ij}$ are related to the elastic constants $C_{ij}$ as:

$$\begin{aligned} S_{11} &= \tfrac{C_{11}+C_{12}}{(C_{11}-C_{12})(C_{11}+2C_{12})}, \\ S_{12} &= \tfrac{-C_{12}}{(C_{11}-C_{12})(C_{11}+2C_{12})}, \\ S_{44} &= \tfrac{1}{C_{44}}. \end{aligned} \tag{4.6}$$

Because the holes are induced far away enough from the center of the cavity, the angle $\varphi$ describing the depth of the dot position in the z-direction with respect to the hole is very small and we assume $\cos\varphi \simeq 1$. The strain tensor components become:

$$\begin{aligned} \varepsilon_{xx} &\simeq [1-\eta_1\cos^2\theta]\tfrac{A_0}{r}, \\ \varepsilon_{yy} &\simeq [1-\eta_1\sin^2\theta]\tfrac{A_0}{r}, \\ \varepsilon_{zz} &\simeq \tfrac{A_0}{r}, \\ \varepsilon_{xy} &\simeq -\eta_2\sin\theta\cos\theta\tfrac{A_0}{r}, \end{aligned} \tag{4.7}$$

where $\eta_1 = (1+2C_{12}/C_{11})$ and $\eta_2 = (C_{11}-C_{12})(C_{11}+2C_{12}/(C_{11}C_{44}))$. Strain components $\varepsilon_{yz}$ and $\varepsilon_{xz}$ are very small as they are proportional to $\sin\varphi$.

### 4.5.1 Effect on cavity modes

In Sect. 4.3 we analyzed the frequency change of the cavity mode caused by laser-induced surface defects. The stress generated by the defects (tensor $\sigma_{ij}$) creates strain in the semiconductor material (tensor $\varepsilon_{ij}$), via the elastic compliance tensor $S_{ijkl}$. The strain modifies the optical properties of the material through the elasto-optic tensor $p_{ijkl}$. The change in the dielectric impermeability tensor $B_{ij}$ induced by a hole, for a $4\bar{3}m$ cubic crystal, is:

$$\delta B = \begin{bmatrix} \delta B_{xx} & \delta B_{xy} \\ \delta B_{xy} & \delta B_{yy} \end{bmatrix}, \tag{4.8}$$

with

$$\begin{aligned} \delta B_{xx} &= c_0[\Pi_1\sigma_{xx} - \Pi_2\sigma_{yy}], \\ \delta B_{yy} &= c_0[-\Pi_2\sigma_{xx} + \Pi_1\sigma_{yy}], \\ \delta B_{xy} &= \tfrac{p_{44}}{C_{44}}\sigma_{xy} \end{aligned} \tag{4.9}$$

where $c_0^{-1} = (C_{11}-C_{12})(C_{11}+2C_{12})$, $\Pi_1 = p_{11}C_{11} - p_{12}C_{12}$, and $\Pi_2 = p_{11}C_{12} - p_{12}C_{11}$. Since $B_i = 1/n_i^2$, in the case of the small perturbation,

$$\frac{\Delta n_i}{n} \sim -n^2\frac{\Delta B_i}{2}. \tag{4.10}$$

For a cavity with length $L$ material refractive index $n$, the $m$-th resonant mode wavelength is given by $\lambda_m = 2nL/m$. The refractive indices $n_1$ and

Table 4.1: Material parameters used in the model [93, 99]

| | | GaAs | InAs |
|---|---|---|---|
| Elastic constants ($10^{10}$N/$m^2$) | $C_{11}$ | 11.879 | 8.329 |
| | $C_{12}$ | 5.376 | 4.526 |
| | $C_{44}$ | 5.94 | 3.964 |
| Elasto-optic constants | $p_{11}$ | -0.165 | -0.040 |
| | $p_{12}$ | -0.140 | -0.035 |
| | $p_{44}$ | -0.072 | -0.010 |
| Luttinger parameters | $\gamma_1$ | 6.8 | 20.4 |
| | $\gamma_2$ | 1.9 | 8.3 |
| | $\gamma_3$ | 2.73 | 9.1 |
| Pikus-Bir potentials (eV) | $a_c$ | -7.17 | -5.08 |
| | $a_v$ | 1.16 | 1.00 |
| | $b$ | -1.7 | -1.8 |
| | $d$ | -4.55 | -3.6 |

$n_2$ of the two submodes can be obtained separately from the eigenvalues $B_1$ and $B_2$ of the dielectric impermeability tensor $B$. A spatially uniform change $\Delta n$ in refractive index results in a change in wavelength of the resonant mode $\Delta\lambda_m = \lambda_m(\Delta n/n)$. In order to estimate the isostropic shift of the cavity modes, we take the center of mass of the shift of the two resonance wavelenghts $\Delta\bar{\lambda} = \Delta\lambda_1 + \Delta\lambda_2$. This quantity is proportional to the sum of the eigenvalues of $\delta B$, and does not depend on its off-diagonal elements:

$$\Delta\bar{\lambda} = \lambda_m \frac{n^2}{2}(\delta B_{xx} + \delta B_{yy}) \tag{4.11}$$

$$= \lambda_m \frac{n^2}{2}(p_{11} + p_{12}) \left(1 - \frac{C_{12}}{C_{11}}\right) \left(\frac{A_0}{r}\right). \tag{4.12}$$

An important result is the independence of this quantity from the angle $\theta$ along which the hole is positioned. It therefore allows to compare the effect of different holes on the cavity modes.

With the elastic and elasto-optic coefficients provided in Tab. 4.1 the total wavelength shift is (with $n \sim 3.5$ for GaAs):

$$\overline{\Delta\lambda}[nm] \sim 1100 \frac{A_0}{r}. \tag{4.13}$$

For tensile strain the wavelength redhifts ($A_0$ is positive) and for compressive strain it blueshifts ($A_0$ is negative). Our measurements showed prederentially

a redshift when the cavity is far from polarization degeneracy. Therefore we assume that tensile strain is applied to the material. Experimentally we have little control on the parameter $A_0$ and therefore need to compare it with a similar expression for the QD transition shift.

### 4.5.2 Effect on QD optical transitions

In Chap. 1 Sect. 1.3.3 we described the band structure of III-V semiconductors in the $\mathbf{k}\cdot\mathbf{p}$ approximation. The valence band consists of a doubly degenerate band with angular momentum $j = 1/2$ (spin-orbit split-off band) and two doubly degenerate bands with total angular momentum $j = 3/2$. In the following we neglect the spin-orbit split-off bands which for typical semiconductors are several hundred meV separated from the four $j = 3/2$ bands. These bands contain the light holes (LH) with larger band curvature ($m_j = \pm 1/2$) and the heavy holes (HH) with smaller band curvature ($m_j = \pm 3/2$). The $j = 3/2$ bands can be described by a $4 \times 4$ Luttinger-Kohn Hamiltonian [99], which in the basis $\{|m_z = \frac{3}{2}\rangle, |m_z = \frac{1}{2}\rangle, |m_z = -\frac{1}{2}\rangle, |m_z = -\frac{3}{2}\rangle\}$ writes as:

$$\mathcal{H}_{LK} = \begin{bmatrix} P_k + Q_k & -S_k & R_k & 0 \\ -S_k^* & P_k - Q_k & 0 & R_k \\ R_k^* & 0 & P_k - Q_k & S_k \\ 0 & R_k^* & S_k^* & P_k + Q_k \end{bmatrix}. \tag{4.14}$$

For no strain the coefficients are:

$$\begin{aligned} P_k &= \left(\tfrac{\hbar^2}{2m_0}\right)\gamma_1(k_x^2 + k_y^2 + k_z^2), \\ Q_k &= \left(\tfrac{\hbar^2}{2m_0}\right)\gamma_2(k_x^2 + k_y^2 - 2k_z^2), \\ R_k &= \left(\tfrac{\hbar^2}{2m_0}\right)\sqrt{3}[-\gamma_2(k_x^2 - k_y^2) + 2i\gamma_3 k_x k_y], \\ S_k &= \left(\tfrac{\hbar^2}{2m_0}\right)2\sqrt{3}\gamma_3(k_x - ik_y)k_z, \end{aligned} \tag{4.15}$$

where $\gamma_1$,$\gamma_2$ and $\gamma_3$ are the Luttinger parameters and $m_0$ the free electron mass. In case of applied strain the system can be described by the Pikus-Bir Hamiltonian which has the same form as the Luttinger-Kohn Hamiltonian but with modified coefficients: $P = P_k + P_\varepsilon$, $Q = Q_k + Q_\varepsilon$, $R = R_k + R_\varepsilon$, and $S = S_k + S_\varepsilon$, with

$$\begin{aligned} P_\varepsilon &= -a_v(\varepsilon_{xx} + \varepsilon_{yy} + \varepsilon_{zz}), \\ Q_\varepsilon &= -(b/2)(\varepsilon_{xx} + \varepsilon_{yy} - 2\varepsilon_{zz}), \\ R_\varepsilon &= (\sqrt{3}b/2)(\varepsilon_{xx} - \varepsilon_{yy}) - id\varepsilon_{xy}, \\ S_\varepsilon &= d(\varepsilon_{xz} - i\varepsilon_{yz}). \end{aligned} \tag{4.16}$$

$a_c$,$a_v$,$b$ and $d$ are the Pikus-Bir deformation potentials.

Although accurate theoretical models have been developed to study the complex effect of strain on the energy levels of semiconductor structures [100–103] we elaborate a simplified model two-valence-band model. It should provide a phenomenological understanding of the energy shift of the QD optical transition of use for the experimentalist.

**Two-valence-bands model**

At the their Γ-point ($\mathbf{k} = \mathbf{0}$) the HH and LH valence subbands are degenerate for bulk III-V semiconductors. In low-dimensional structures, such as in self-assembled QDs, this degeneracy is lifted and results in an energy splitting of a few tens of meV. In the following we will neglect this fact and only consider the conduction band and the HH valence band trying to get a qualitative explanation of the results for the band edge ($\mathbf{k} = \mathbf{0}$).

In the effective mass and envelope function approximation [99], the wave function of a single particle in a QD can be described by the product of a Bloch function $u_k(r)$ with the periodicity of the atomic lattice, and an envelope function $f(r)$, which describes the amplitude modulation of the wave function that is imposed by the confinement potential:

$$\psi(r) = f(r)u_k(r). \tag{4.17}$$

The effective masses for the electrons are $m^*_{e,t} = m^*_{e,z} = m_0/\gamma_e$, and for the heavy holes $m^*_{h,t} = m_0/(\gamma_1 + \gamma_2)$ and $m^*_{h,z} = m_0/(\gamma_1 - 2\gamma_2)$, where $m_0$ is the free-electron mass.

If we assume the QDs to be smaller than the corresponding bulk exciton radius ($\sim$ 35nm for InAs, $\sim$ 15nm for GaAs), the strong-confinement approximation applies. Hence, we treat electrons and holes as independent particles with their energy primarily determined by the confinement potential, and neglect or treat the electron-hole Coulomb potential as a perturbation [104–106].

Consider a QD spherically symmetric in the $x, y-$plane with width $2L_t$ and depth $2L_z$ along the growth axis $z$. The resulting potential is schematically shown in Fig. 4.14. At low temperatures the energy gap is $E_g = 1.52$eV for GaAs and $E_g = 0.42$eV for InAs. Taking the valence-band offset to be $V_h^{(o)} = 0.25$eV [99] leaves $V_c^{(o)} = 0.87$eV for the conduction-band offset. Neglecting the Coulomb interaction as mentioned, the exciton energy is

$$E_0 = E_g^{(0)}(\text{InAs}) + E_v^{(o)} + E_c^{(o)}, \tag{4.18}$$

with $E_v^{(o)}$ and $E_c^{(o)}$ being the ground-state energies for the potential wells of the conduction and valence wells.

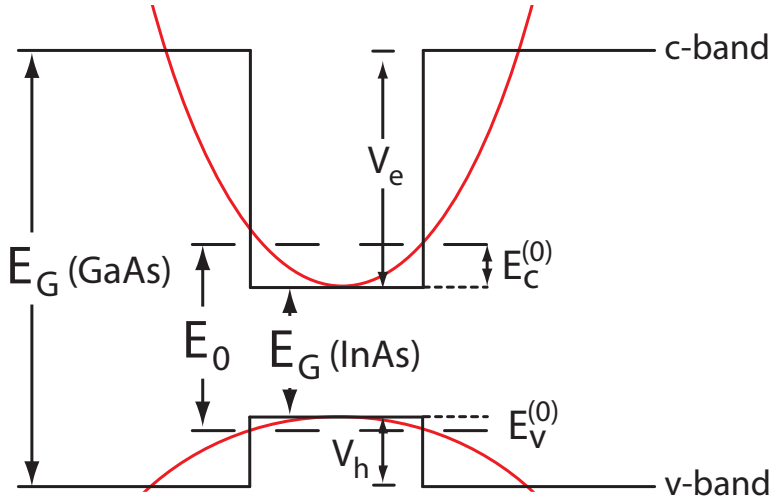


Figure 4.14: *Schematic band structure approximation for a QD at the band edge (*$\mathbf{k} = \mathbf{0}$*).*

A simple analytical solution can be obtained approximating the potential well with a three-dimensional parabolic potential [106]:

$$V_i(r) = \frac{1}{2}c_{i,t}(x^2 + y^2) + \frac{1}{2}c_{i,z}z^2, \quad i = e, h. \tag{4.19}$$

Approximating the square finite well with the parabola yields the coefficients $c_{i,j}$:

$$\frac{1}{2}c_{i,j}L_j^2 = \frac{V_i}{2}, \tag{4.20}$$

resulting in $c_{i,j} = V_i/L_j^2$ and $\Omega_{i,j} = (1/L_j)\sqrt{V_i/m_{ij}^*}$. While index $i$ spans the conduction and valence bands ($i = e, h$), $j$ identifies either the transverse coordinate in the $xy-$plane ($j = t$) or along the growth direction ($j = z$). $m_{ij}^*$ is the effective mass for the electron ($i = e$) or the hole ($i = h$) in the InAs potential well along the $j$ direction. The ground-state energy for the parabolic potential well is

$$E_i^{(0)} = \frac{\hbar}{2}(\Omega_x + \Omega_y + \Omega_z), \tag{4.21}$$

which gives

$$\begin{aligned} E_c^{(o)} &= \tfrac{\hbar}{2}\sqrt{\tfrac{V_e}{m_0}}\left(\tfrac{2}{L_t} + \tfrac{1}{L_z}\right)\sqrt{\gamma_e}, \\ E_v^{(o)} &= \tfrac{\hbar}{2}\sqrt{\tfrac{V_e}{m_0}}\left(\tfrac{2}{L_t}\sqrt{\gamma_1 + \gamma_2} + \tfrac{1}{L_z}\sqrt{\gamma_1 - 2\gamma_2}\right). \end{aligned} \tag{4.22}$$

The parabolic approximation is excellent for the potential well in the $xy-$plane [107, 108]. Along the $z-$axis, the potential well is more abrupt and the approximation not so accurate but sufficient for our qualitative understanding.

If the laser induces strain in the material, the band edges are modified as $E_c = E_c^{(o)} + \Delta_e$ and $E_v = E_v^{(o)} + \Delta_h$, with

$$\begin{aligned} \Delta_e &= a_c \varepsilon_H, \\ \Delta_h &= a_v \varepsilon_H + \tfrac{b}{2} \varepsilon_B \end{aligned} \tag{4.23}$$

With the expression for the strain tensor components derived in Eq.(4.7), for the hydrostatic strain component $\varepsilon_H$ we get

$$\varepsilon_H = \varepsilon_{xx} + \varepsilon_{yy} + \varepsilon_{zz} = 2 \left( \frac{A_0}{r} \right) \left( \frac{1 - C_{12}}{C_{11}} \right), \tag{4.24}$$

and for the biaxial component (assuming $\varphi \approx 0$)

$$\varepsilon_B = \varepsilon_{xx} + \varepsilon_{yy} - 2\varepsilon_{zz} = - \left( \frac{A_0}{r} \right) \left( \frac{1 + 2C_{12}}{C_{11}} \right). \tag{4.25}$$

This yields

$$\begin{aligned} \Delta_e &= 2a_c \left( 1 - \tfrac{C_{12}}{C_{11}} \right) \left( \tfrac{A_0}{r} \right), \\ \Delta_h &= \left[ 2a_v \left( 1 - \tfrac{C_{12}}{C_{11}} \right) - \tfrac{b}{2} \left( 1 + 2\tfrac{C_{12}}{C_{11}} \right) \right] \left( \tfrac{A_0}{r} \right). \end{aligned} \tag{4.26}$$

It is interesting to note that the strain components affecting the conduction band and the heavy-hole valence band are independent of the relative angle $\theta$. This agrees with the redshift measured for several QD optical transitions at different angles $\theta$ but with the same distance from the cavity center, see Fig. 4.12(b).

The perturbation in the band energies for the conduction and valence bands for GaAs and InAs has two consequences. First, the bandgap energy of InAs is modified as

$$E_g(\text{InAs}) = E_g^{(0)}(\text{InAs}) + \Delta E_g, \tag{4.27}$$

with

$$\Delta E_g = \Delta_e(\text{InAs}) - \Delta_h(\text{InAs}) = (a_c - a_v)\varepsilon_H - \frac{b}{2}\varepsilon_B. \tag{4.28}$$

Second, the depth of the potential wells is modified, due to the relative shift between GaAs and InAs band edges, giving a perturbation on the ground-state

energies of the potential wells (respectively $\Delta E_c$ and $\Delta E_v$). The confining potential for the electron is modified to

$$V_e = V_e^{(o)} + \delta_e \left( \frac{A_0}{r} \right), \tag{4.29}$$

with

$$\delta_e \left( \frac{A_0}{r} \right) = \Delta_e(\text{GaAs}) - \Delta_e(\text{InAs}). \tag{4.30}$$

For the holes we get

$$V_h = V_h^{(o)} + \delta_h \left( \frac{A_0}{r} \right), \tag{4.31}$$

with

$$\delta_h \left( \frac{A_0}{r} \right) = \Delta_h(\text{GaAs}) - \Delta_h(\text{InAs}). \tag{4.32}$$

Substituting the new expression for the confining potential in the ground-state energies in Eq.(4.22) and applying a first-order Taylor expansion (the perturbation due to a hole burned is very small), yields

$$\Delta E_i = \xi_i \delta_i \left( \frac{A_0}{r} \right), \quad i = c, v. \tag{4.33}$$

The $\delta_i$ depend on the elastic properties of the materials, namely the elastic constants and the deformation potential. The $\xi_i$ depend on the band structure:

$$\begin{aligned} \xi_c &= \tfrac{\hbar}{2} \left( \tfrac{1}{L_z} + \tfrac{2}{L_t} \right) \sqrt{\tfrac{\gamma_e}{m_o V_e^{(o)}}}, \\ \xi_v &= \tfrac{\hbar}{2} \left( \tfrac{1}{L_z} \sqrt{\gamma_1 - 2\gamma_2} + \tfrac{2}{L_t} \sqrt{\gamma_1 + \gamma_2} \right) \sqrt{\tfrac{1}{m_o V_h^{(o)}}}. \end{aligned} \tag{4.34}$$

Let us consider an example with typical QD parameters as used in our samples. A QD with a thickness of 3nm and a width of 12nm ($L_z = 1.5$nm and $L_t = 6$nm), we get $\xi_e \sim 1.224$ and $\xi_h \sim 1.031$. Using the values given in Tab.4.1, we get $\Delta_e(\text{InAs}) \sim -4.638\text{eV}(A_0/r)$ and $\Delta_h(\text{InAs}) \sim 2.791\text{eV}(A_0/r)$. In the case of compressive strain, this yields an increase for the bandgap energy of InAs because $E_g[\text{InAs}] = E_g^{(0)}[\text{InAs}] + 7.43\text{eV}(A_0/r)$. For tensile strain the energy decreases by the same amount. The shift in the GaAs conduction band is $\Delta_e(\text{GaAs}) \sim -6.546\text{eV}(A_0/r)$, so that the change in depth of the potential well is $\delta_e(A_0/r) = -1.91\text{eV}(A_0/r)$. In the same way, the shift for the valence band is $\Delta_h(\text{GaAs}) \sim -2.678\text{eV}(A_0/r)$, with a change in the depth of the corresponding potential well of $\delta_h(A_0/r) = 0.113\text{eV}(A_0/r)$. For both, conduction and valence band, the depth of the potential well is increased by

compressive strain and reduced by tensile strain. The effect is much stronger for the conduction band than for the valence band.

If we want to quantify the redshift of the QD optical transition due to applied tensile strain, we have to take both the change in InAs energy gap and in the pontential well depth into account. A redshift due to hole-burning by an amount of $\Delta E \sim -9.78\text{eV}(A_0/r)$ results in the following wavelength shift:

$$\Delta\lambda[nm] \sim 7800\frac{A_0}{r}. \tag{4.35}$$

In our measurements, a typical redshift due one induced hole is about $100\mu$eV. This implicates that the value for $(A_0/r)$ is in the order of $10^{-5}$, which in turn corresponds to a shift of the InAs bandgap of around $75\mu$eV. The change in the conduction-band confinement potential is around $\delta_e(A_0/r) \sim -20\mu$eV and for the valence-band confinement well $\delta_h(A_0/r) \sim -1\mu$eV.

**Comparison of the cavity and the QD effects**

Comparing the relative magnitude $\eta$ of the effects for the QD transition and the cavity mode, with Eq.(4.35) and Eq.(4.13) we get:

$$\eta = \frac{\Delta\lambda_{QD}}{\Delta\lambda_{cav}} \sim 6. \tag{4.36}$$

Experimentally we measured $\eta$ to be in average around 5 (see Fig. 4.13). From Eq.(4.33) we know that $\eta$ depends on the elastic properties of the material and on $L_z$ and $L_t$. However, the dependency on the latter parameters is weak. For emission energies ranging between 1 and 1.5eV and QD sizes with a thickness of 2 to 4nm ($L_z = 1$ to 2nm) and a width of 8 to 16nm ($L_t = 4$ to 8nm) $\eta$ is bound between 5.5 and 7.

## 4.6 Conclusion and discussion

Tuning micropillar cavity modes and the optical transitions of embedded QDs by laser-induced surface defects allows to obtain a polarization-degenerate fundamental mode to be in resonance with the QD optical transition. Advantages over other techniques are the precise control inducing permanent changes. We can tune QD optical transitions in micropillars that are not directly accessible from the surface leaving the quality of the QD intact. There is no need to alter the experimental setup for further measurements once the cavities have been tuned.

Because of the agreement of the qualitative predictions by the theoretical model with the experimental results, we believe that the holes burned induce tensile strain on the QDs. This could be explained assuming removal of material which releases some compressive strain that pre-exists due to lattice-mismatch in the QD. Such tensile strain affects the band-structure both of the InAs QD material and of the bulk surrounding GaAs, reducing the InAs energy gap and the width of the confining potential well.

A question that comes to mind is about the resistance of the samples towards the induced heat. We have tested the hole burning technique with much higher powers (up to 800mW at 4K) and for much longer times (up to 3 minutes) than required and have seen the temperature sensor at the sample holder increase up to 12K. These tests never resulted in a clear degeneration of the samples. However, one important sample degraded almost instantly between one and the other cooldown. In the past other samples have also been significantly changed after a thermal cycle. This seems to indicate that the hole burning method is less damaging than thermal cycling from 4K to room temperature.